applied sciences

MDPI

Article

CFD Study of the Impact of an Electrical Power Transformer on a Historical Building: Assessment and Solutions

Fabio Nardecchia [1], Luca Gugliermetti [2], Laura Pompei [1,*] and Federico Cinquepalmi [2]

[1] Department of Astronautic, Electric and Energy Engineering (DIAEE), Faculty of Engineering, Sapienza University of Rome, Via Eudossiana 18, 00185 Rome, Italy; fabio.nardecchia@uniroma1.it
[2] Department of Architecture and Design (DIAP), Faculty of Architecture, Sapienza University of Rome, Via Flaminia 359, 00185 Rome, Italy; luca.gugliermetti@uniroma1.it (L.G.); federico.cinquepalmi@uniroma1.it (F.C.)
* Correspondence: laura.pompei@uniroma1.it

Abstract: Historical building reuse is aimed at preservation, where buildings are recovered for new uses connected to cultural activities. This paper presents the analysis of the impact of thermo-fluid dynamics due to a 500 kW electrical power transformer installed inside a historical building. The analysis is performed using computational fluid dynamics simulations validated through measurement campaigns carried out during the summer period. High temperatures and wide humidity variations can damage building plasters and cause malfunctions in power equipment. To avoid these situations, two different installation layouts were studied. One consists of the power transformer directly installed in the environment and cooled by an inlet fan, and the other consists of the power transformer being insulated from the external environment by an enclosure connected to a forced ventilation system. The second layout showed better results both inside and outside the transformer enclosure. The maximum indoor condition was about 4.3 °C, with a −7.2% RH and an airflow rate of 1100 m^3/h, and the maximum outdoor air condition was 3.3 °C, with a −1.39% RH and a flow rate of 2200 m^3/h. However, the temperatures and humidity inside the building and outside the transformer enclosure were almost the same.

Keywords: building; indoor environmental analysis; power systems; forced ventilation; preservation; computational fluid dynamics

Citation: Nardecchia, F.; Gugliermetti, L.; Pompei, L.; Cinquepalmi, F. CFD Study of the Impact of an Electrical Power Transformer on a Historical Building: Assessment and Solutions. *Appl. Sci.* **2024**, *14*, 10827. https://doi.org/10.3390/app142310827

Academic Editor: Rafael Royo-Pastor

Received: 23 September 2024
Revised: 11 November 2024
Accepted: 20 November 2024
Published: 22 November 2024

1. Introduction

Natural and forced ventilation in historical buildings is widely discussed among researchers [1]. Most ancient buildings and villages are today renovated to be used as cultural places such as museums, exhibitions, and cultural centers, or to host government buildings, public services, and administrations [2,3]. It can be difficult to renovate the interior environment of such buildings due to the restrictions of national regulations for historical structures that usually forbid structural interventions, especially those relating to facades or elements of historical value (i.e., fixtures, windows, doors) [4]. Moreover, these restrictions must deal with the final use of the building. These restrictions, together with the severity of hot climates, can raise the difficulty of managing indoor hygrothermal conditions (air temperature and relative humidity). Some other fundamental elements associated with good hygrothermal control are thermal masses, the shape of the building, the number of occupants, the power dissipated, the wind conditions, the solar irradiation, shading, and the materials used [5,6].

Ancient buildings were typically not designed to host active conditioning or ventilation systems [7] but natural ventilation, using holes, windows, and skylights [8,9]. Some cultures developed rudimental heating systems; for example, the Romans and Greeks used hypocaust baths [10], China had the kang and dikang, and Korea had the ondol [11,12], which all employed underfloor tubing systems to heat the environments with a furnace.

Adding a new conditioning system in an ancient building can lead to negative impacts on the asset's cultural preservation, altering the building itself and potentially changing the delicate interior environmental conditions [13,14]. At the same time, uncontrolled and quick variations in temperature and moisture can damage both the cultural goods contained and the building itself. A common example is the condensation of water on walls, which can lead to molds and lichens growing, resulting in damage to mortars and plasters [15]. Even low humidity can be dangerous, as it can raise water from the wall and cause saline formations. These issues are related to the final use of the building; for example, for a museum, it depends on the number of visitors, and in the case of administrative or government buildings, it is related to the thermal power dissipated inside the environment and the hygrothermal comfort requirements. Rosina [14] investigated the variation in thermal and humid conditions during the burial of a tomb, from the closure of the tomb to its excavation, by field testing and Computational Fluid Dynamics (CFD) modelling.

As highlighted by the authors, dramatic changes in the thermal and humid environment will speed up the deterioration of historical artefacts [13]. Nowadays, CFD modelling is widely adopted as a tool for simulating indoor hygrothermal parameters. However, developing an accurate CFD model for historical buildings can be challenging [16]. Corgnati and Perino [17] employed CFD modelling to analyze the best ventilation strategy to be used inside the "Senate Room" at "Palazzo Madama", an 18th-century building. As a result, they revealed the possibility of using a Heating, Ventilation and Air Conditioning system (HVAC) to manage the thermal loads due to the large exhibitions inside the palace. Another example was developed by Balocco and Grazzini [18], which used a CFD model, based on measured data, to assess the performance of an HVAC installed in the "Hall of the Five Hundred" at "Palazzo Vecchio" in Florence. Abuku et al. [19] developed another CFD model to evaluate the effects of wind-driven rain on building parameters such as hygrothermal response, the rate of mold growth on wall surfaces and energy consumption. Gagliano et al. [20] investigated the "Indirizzo" Baths of Catania (Sicily), which represent one of the best-preserved Roman thermal baths. Using CFD simulations, they assessed the indoor thermal condition of the environment. Balocco [21] developed an integrated CFD model able to consider the relationship between indoor and outdoor environments, lighting, occupancy, and HVAC systems. The list of scientific papers that use CFD to simulate the thermo-hygrometric conditions inside ancient buildings is extensive [22–27].

In this framework, this study is oriented to a very specific topic, namely the investigation of the effect of an electrical transformer enclosure placed inside an ancient Roman building. This work paves the way for analyzing the variation in the ancient building's indoor environment due to the installation of an electric transformer enclosure. The decision to use a historical building for this study could be surprising. But due to the Archaeological Park of the Colosseum, at the center of Rome, near the Roman Forum of Trajan, there are no other places wherein the electrical transformer enclosure could be installed. A new building could alter the sight of the ancient ruins, altering the park's appearance. At the same time, the underground is full of buried ruins, making it impossible to create a new underground environment to host the transformer enclosure. Therefore, it could only be placed inside an existing Roman building.

To guarantee the indoor hygrothermal conditions of the ancient Roman building (named "Museeto") due to the presence of an electrical transfer enclosure, different analyses were carried out. Firstly, an experimental campaign was carried out to collect environmental data using outdoor and indoor sensors. The campaign was carried out during the warmest months, from July to September (19 July 2020–17 September 2020), to investigate the worst operating conditions and the maximum overheating that could be achieved during the year. Then, the collected data were used to validate a CFD model and two different layouts for the electrical transformer enclosure were simulated. They differ by the presence of an enclosure layer between the electric transformer system and the indoor environment. Moreover, two different flow rates, 2200 m^3/h and 1100 m^3/h, were used to assess the

internal temperature and humidity over the year. The two flow rates were chosen by the company in charge of the cabin's design for the Archaeological Park of the Colosseum.

This paper starts with the identification of the ancient building named "Museéto". This section contains all the information related to the building itself and the measurement campaign. Then, the CFD model set-up is presented, as well as the validation of the model based on the measurement campaign data; two different transformer enclosure layouts are introduced and simulated. One has the power transformer placed in an open configuration, and the other has the power transformer placed within a confined environment. Finally, the results are presented, and the main relevant findings are discussed, with a comparative analysis of the advantages and disadvantages related to the two configurations.

2. Materials and Methods

2.1. Case Study: "Museeto" Building, Archaeological Park of the Colosseum

The site selected to host the electric transformer enclosure is called "Museéto", a building located on the street named "via Sacra". The age of the building is unclear, but it is supposed to have been built during the 3rd century A.D. The area wherein the building is located has undergone complex topographic development. Since the archaic age, the area has experienced many building phases, which makes it difficult to date the building complexes chronologically. After the Neronian fire, the construction of long porches and arches changed the appearance of "via Sacra", creating a monumental asset for the nearby Roman Forum. The "Museéto" building belongs to a later period, and it is the best-preserved building in the local complex (probably comprising a total of nine buildings alternated by travertine floors). The complex was probably built during the 2nd century A.D., together with a sidewalk near the temple of "Casa delle Vestali", leaning against the pillars of the portico. The discovery of the area was made by G. Boni at the end of the 19th century [28]. The area was demolished during the 3rd century to build three new rooms with an almost square plan protruding towards the street "Via Sacra". The sidewalk was occupied and the passage to the portico area was closed off by walls. This transformation has been dated to the 3rd century, based on the ceramic material found and on the building technique. Access to the rooms was by a common corridor made of travertine slabs, accessible from "Via Sacra". At the end of the 3rd century A.D., the rooms were demolished again and replaced by perhaps four more new rooms. The only environment visible in elevation today, including the modern restored roof, is the "Museéto". The supposed scope of these environments varies from a more generic "Taberna" to a "Stàtion" [29], a term associated with the names of cities in the eastern Mediterranean in Greek inscriptions [30]. The main hypothesis about the complex is that they were "stationes exterarum civitatum" (stations of foreign states, in Latin), established for commercial purposes and/or for carrying out ritual activities. Unlike the other buildings, "Museéto" was not subjected to structural changes in the subsequent transformation phase of the 4th century. It was probably used as an "apodyterium" (locker room).

Architectural Description

The building consists of a single room featuring a niche in the back wall. The curtain is constructed from dark yellow bricks of varying dimensions, ranging from 11.6 to 29.7 cm in length (with an average of 18.3 cm) and from 2.3 to 3.4 cm in height (with an average of 2.8 cm). These bricks contain numerous chamotte inclusions and small vacuoles. The row mortar material is irregular, with a thickness of up to 3 cm; it is gray and likely made from a mix of gray and red pozzolana, appearing to be unstyled. The structure exhibits signs of wall renovations, probably carried out during the medieval period.

The room measures approximately 4 × 8.35 × 4.68 m (width × length × height) and features a skylight window in the ceiling, likely installed when the building was converted for museum use. Access to the room is provided by a recent door measuring approximately 1.44 m. Additionally, there is a small niche, measuring 0.6 m, located halfway up the wall at the back of the room. The dimensions are illustrated in the sections and plans

shown in Figure 1. In the floor plan, three environmental sensors are shown, as described in Section 2.2.

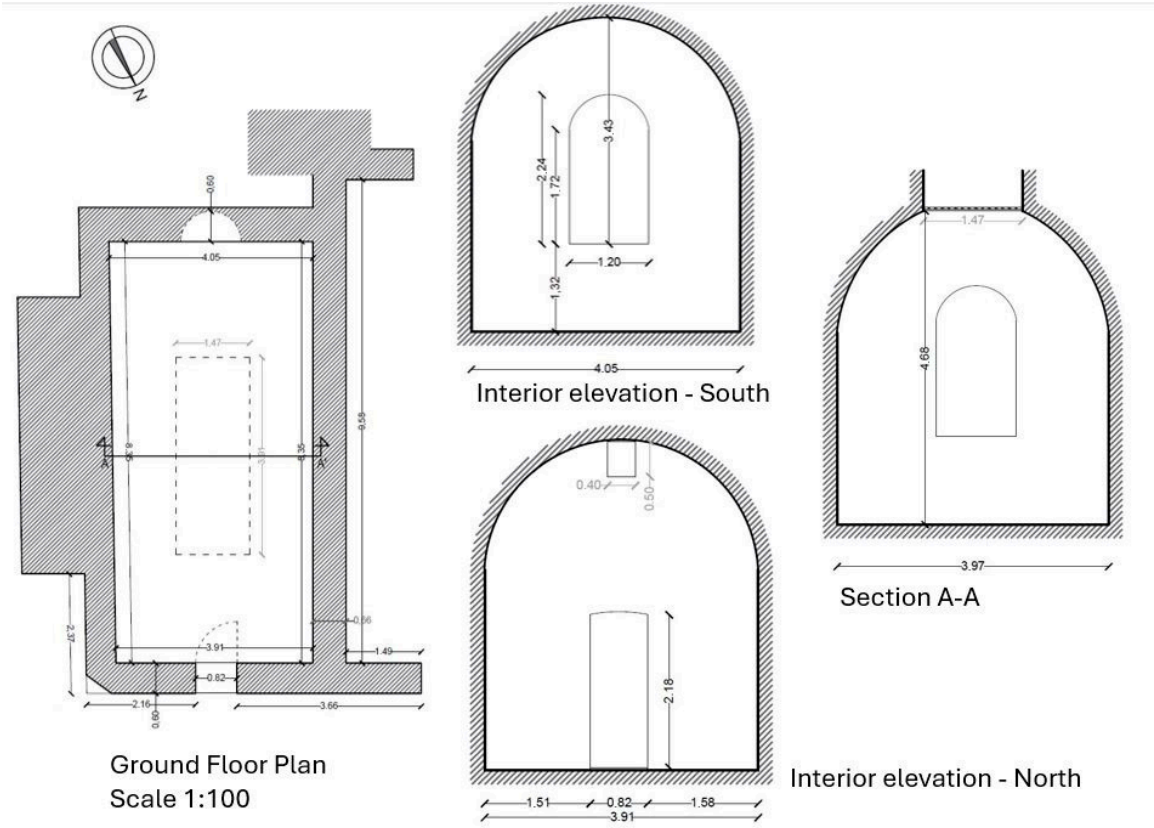

Figure 1. Museéto architectural plan with three sections at the beginning, middle and end of the room.

All the measurements were made with the laser Liner Diameter Measurement (LDM) model Leica S910 with an error < ±0.1 cm/m. Moreover, the building a shows a little expansion, with the upper part of the walls being approximately 1 mm wider than the lower part. This is probably due to the presence of external buttresses on only one side of the structure and the thrust of the vaults.

2.2. Environmental Measurements and Uncertainties

To validate the CFD simulation, an experimental campaign was conducted. Data were collected from three different sensors and an external weather monitoring system over a period of approximately two months (from 19 July 2020 to 17 September 2020). The weather monitoring station used was the DA-VIS® VANTAGE PRO2 model (Davis, Newport Beach, CA, USA). It was installed with a wind sensor on the roof of the building to minimize interference in the wind speed and direction measurements. The body of the weather station was positioned on the side, approximately 2.5 m away from the building, in a location that concealed it as much as possible from the view of tourists.

The measurement errors, as declared by the manufacturer of the weather station, are reported in Table 1.

During the same period, the indoor climate was also monitored for thermo-hygrometric conditions as part of the experimental campaign. Three sensors were installed within the structure: two located in the middle of the side walls (Sensors 72 and 84) and one positioned at the center of the room (Sensor 66). All sensors were set at an approximate height of 1.70 m above the ground (refer to Figure 1). The sensors utilized were "VOLTCRAFT® DL-121TH Multifunctional Data Loggers (VOLTCRAFT, Las Vegas, NV, USA)", with their measurement uncertainties provided in Table 2.

Table 1. DAVIS VANTAGE PRO2 measurement errors (source: Datasheet).

Variable	Value
Pressure	±1.0 hPa
Dewpoint	±1 °C
Humidity	±2% RH
Rainfall	The higher between 250 mm/h and ±3%
Solar Radiation	±5% of full scale
Temperature	±0.3 °C
Wind Direction	±3°
Wind Speed	±0.9 m/s

Table 2. VOLTCRAFT DL-121TH measurement errors (source: Datasheet).

Variable	Value
Humidity	±3% RH
Temperature	±1 °C

This type of data logger is particularly compact, allowing it to be used without an external power supply thanks to an integrated lithium battery. With a single battery change, they can acquire up to 16,000 temperature and 16,000 humidity measurement values.

2.3. Outdoor Conditions

The outdoor environmental conditions were monitored using the weather station, and the data were collected via the WeatherLink Cloud® online service. This program automatically compiles a data log file that records the average weather conditions measured every 15 min in GMT+1. As shown in Figure 2, the highest temperature recorded during the experimental campaign was 39 °C on 31 July 2020 at 15:45, while the lowest was 16.2 °C on 1 September 2020, at 06:45. The average temperature throughout the campaign was 27.7 °C. The temperature trends were fairly consistent, with only one notably colder day (1 September 2020). A rainy day occurred on 31 August 2020, with a total of 10 h of precipitation, amounting to 13.8 mm of rainfall. The humidity levels also remained relatively stable, reaching a maximum of 91% RH on the rainy day (31 August 2020) and a minimum of 25% RH on 25 July 2020, at 15:00, on 9 August 2020, at 13:30 and 14:45, and on 13 August 2020, at 15:00. The average humidity was 58.42% RH. The dew point, as calculated by the software, indicated a maximum of 24.4 °C (31 July 2020, at 23:00), a minimum of 10.7 °C (5 August 2020, at 14:45), and an average of 18.2 °C. Daily variations, due to the night–day cycles, showed an average range of 12.5 °C for outdoor temperature, 43.8% RH for humidity, and 4.1 °C for the dew point.

The solar radiation measured during the campaign is shown in Figure 3. As can be seen, most of the measurements were taken on sunny days, except for one rainy day (31 August 2020) and one cloudy day (11 September 2020). The maximum solar radiation measured flux was 928 W/m^2 on 25 July 2020 at 13:15, and the average daily value (between 8:00 and 20:00) was 573.6 W/m^2.

The Wind Rose chart of the reference period is shown in Figure 4a. As can be seen, the main wind directions were North-East and West-South-West, with the strongest wind from the North-East (>5km/h). Wind depends on the surrounding environment, and the building is located below the level of the street in a cavity surrounded by buildings. This limits the wind direction as well as its intensity. As can be seen in Figure 4b, the average wind speed in km/h comes from the North-East, South-West and South-East with about the same intensity (4–4.3 km/h).

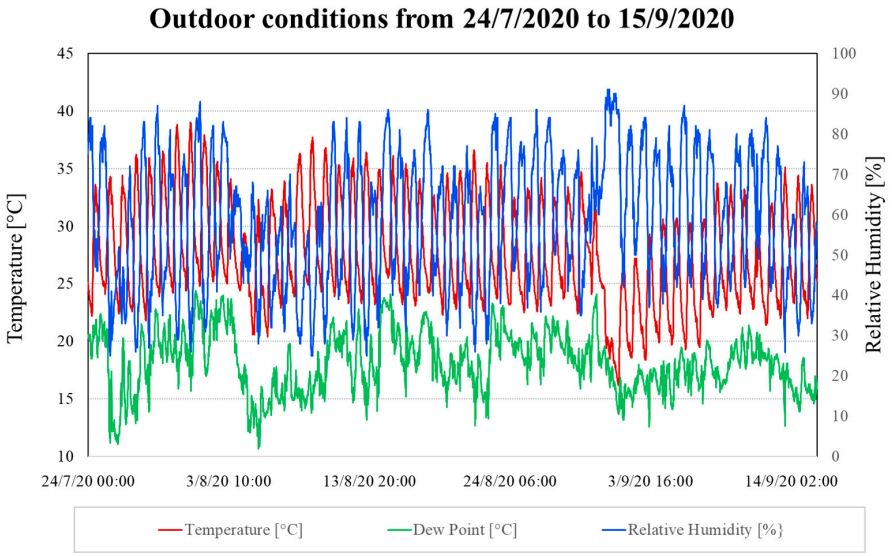

Figure 2. Environmental data (Temperature [°C], Relative Humidity [%RH] and Dew Point [°C]) collected by the weather station during the period from 24 July 2020 to 15 September 2020.

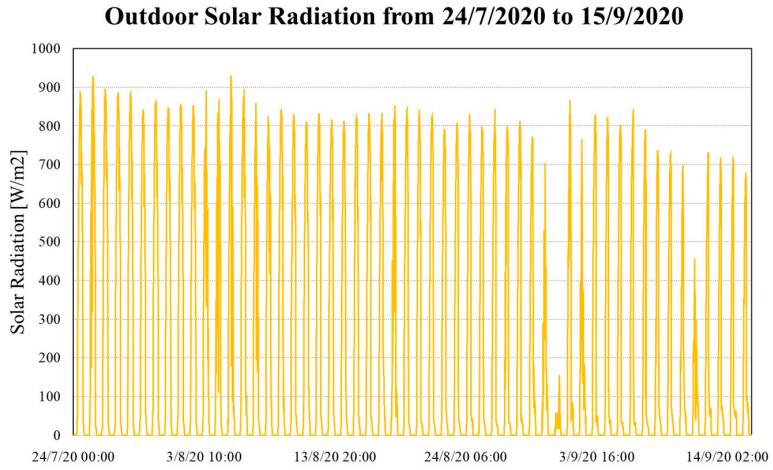

Figure 3. Solar radiation [W/m^2] measured by the weather station during the period from 24 July 2020 to 15 September 2020.

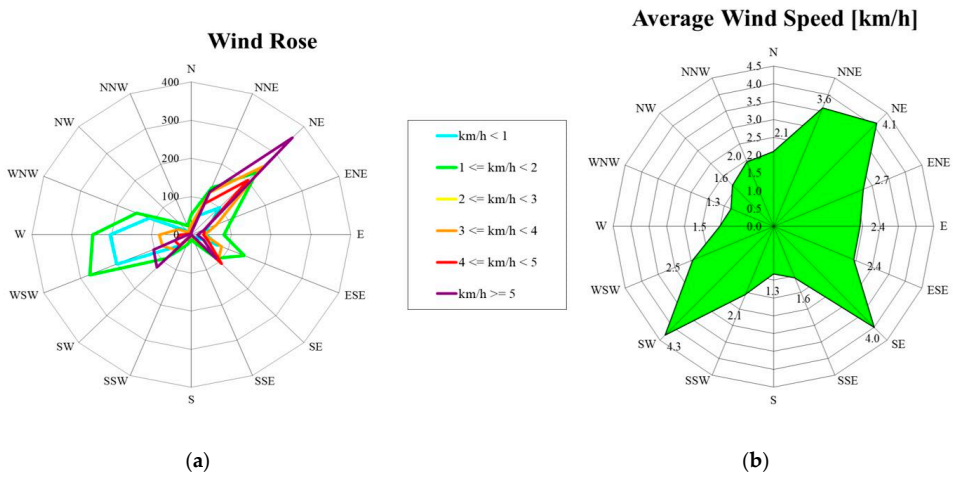

(**a**) (**b**)

Figure 4. (**a**) Wind Rose chart with principal wind components (in [km/h]) measured by the weather station during the period from 24 July 2020 to 15 September 2020; (**b**) Average wind speed components (in [km/h]) measured by the weather station during the period from 24 July 2020 to 15 September 2020.

2.4. Indoor Conditions

The indoor conditions were monitored using three multifunctional data loggers labeled 66, 72, and 84. Data collection was conducted using the VOLTCRAFT® software suite. The trends from the central sensor (number 66) are presented in Figure 5, reflecting the average room conditions. Sensors 72 and 84 were placed near the wall to monitor the temperature at the boundary conditions for the simulation assessment (Figure 5).

The influence of external weather is clearly visible, particularly on the rainy day of 31 August 2020, when the temperature dropped by 5.5 °C. Additionally, the day–night cycles exhibited a reduced sinusoidal variation compared to the outside, with an average difference of 4 °C and 10% RH. The maximum recorded temperature indoors was 32.4 °C on 31 July 2020, at 12:35, which corresponded to the outdoor maximum with a delay of approximately 2 h and 45 min. Conversely, the minimum indoor temperature of 23 °C occurred on 1 September 2020, at 08:35, also matching the outdoor temperature with a delay of about 1 h and 45 min. The mean temperature throughout the experimental campaign was 28.4 °C, which is 0.7 °C lower than the measurement uncertainty for both the indoor and outdoor temperature sensors (±1.3 °C). The relative humidity varied from a maximum of 70.4% RH on 29 July 2020, at 03:05 to a minimum of 44.8% RH on 22 August 2020, at 15:05, with an average of 58.9% RH; this is 0.5% RH higher than outside and within the error bands of the instruments (±5% RH). The dew point, critical for conservation, was calculated by the software and showed a maximum of 23.9 °C on 2 August 2020, at 22:05, and a minimum of 14.9 °C on 26 June 2020, at 05:35, with an average value of 19.5 °C.

Sensor 72 was installed on the North-West wall, which is thinner compared to the South-East wall. This difference results in higher temperatures and creates sharp peaks in the maximum temperature readings. The highest temperature recorded by this sensor was 34.3 °C on 25 July 2020, at 10:35, while the lowest was 23.8 °C on 1 September 2020, at 09:05, leading to an average temperature of 28.6 °C. For dew point temperatures, the maximum measured was 24.5 °C on 3 August 2020, at 00:05, and the minimum was 15.2 °C on 5 August 2020, at 00:05, with an average of 19.9 °C. The humidity readings showed a maximum of 71.9% RH on 9 July 2020, at 02:35, a minimum of 43.6% RH on 26 July 2020, at 10:35, and an average of 59.6% RH.

Sensor 84 was located on the South-East wall, which has the greatest thickness compared to the other walls. This increased thickness provides better insulation and greater thermal inertia, leading to lower wall temperatures and a longer thermal response time. For this sensor, the maximum temperature recorded was 32.1 °C on 31 July 2020, at 12:35, while the minimum was 24.1 °C on 1 September 2020, at 08:35, with an average of 28.7 °C. The temperature variability is slightly lower, with a range of 8 °C between the minimum and maximum readings, compared to 10.5 °C for the North-West wall and 9.4 °C in the center of the room. This reduced variability is likely due to the better insulation. Additionally, the maximum temperature was not reached on the same day. The absolute minimum temperature was recorded in the center of the room, possibly influenced by the roof skylight. The relative humidity for this sensor peaked at 71.6% RH on 15 August 2020, at 06:05, dropped to a minimum of 48.1% RH on 26 July 2020, at 18:35, and averaged 61.2% RH. For the dew point temperatures, the maximum recorded was 24.5 °C on 2 August 2020, at 21:33, and the minimum was 16.1 °C on 26 July 2020, at 06:35, with an average of 20.4 °C. All measured maximum, minimum, and average values are summarized in Table 3 for convenience.

A delay in the propagation of the heat wave is visible from the dates reported in Table 3, where minimum and maximum temperatures were reached during different times of the day. The only exception is for the maximum temperature measured on the North-West-facing wall, which reached its maximum at a different moment, on a day with a solar radiation peak (25/7/20). The other temperatures followed the same trends as the outdoor environment. Finally, the relative humidity and dew points show longer trends due to the time needed for the water to diffuse inside the building's walls and ceiling.

Table 3. Outdoor and indoor environmental conditions during the period from 24 July 2020 to 15 September 2020.

	Outdoor			Centre of the Room			South-East Wall			North-West Wall		
	Max.	**Avg.**	**Min.**	**Max.**	**Avg.**	**Min.**	**Max.**	**Avg.**	**Min.**	**Max.**	**Avg.**	**Min.**
Temp. [°C]	39	27.7	16.2	32.4	28.4	23.9	32.1	28.7	24.1	34.3	28.6	23.8
Date	31/7/20 15:45	-	1/9/20 06:45	31/7/20 12:35	-	1/9/20 8:35	31/7/20 12:35	-	1/9/20 8:35	25/7/20 10:35	-	1/9/20 9:05
Humidity [$\%_{RH}$]	91	58.4	25	70.4	58.9	44.8	71.6	61.2	48.1	71.9	59.6	43.6
Date	25/7/20 15:00		9/8/20 13:30–14:45 13/8/20 15:00	29/7/20 3:35	-	22/8/20 15:05	15/8/20 6:05	-	26/7/20 18:35	29/7/20 2:34	-	16/7/20 10:34
Dew point [°C]	24.4	18.2	10.7	23.9	19.5	14.9	24.5	20.4	16.1	24.5	19.9	15.2
Date	31/7/20 23:00	-	5/8/20 14:45	2/8/20 22:05	-	26/7/20 5:33	2/8/20 21:35	-	26/7/20 6:35	3/8/20 00:05	-	5/8/20 00:05

2.5. CFD Model Setup

For the CFD simulation, the commercial software Ansys Fluent v.14.5 was utilized [28]. This software is widely recognized within the scientific community due to its reliability and precision. Its key features include a 3D double-precision solver, a pressure-based solver, steady-state analysis, and RANS (Reynolds-averaged Navier–Stokes) equations combined with the standard RNG k-ε model [29]. The PISO algorithm [30] was employed for pressure–velocity coupling. Pressure interpolation schemes were chosen for the convection and viscous terms of the equations, utilizing second-order discretization schemes. During the simulation, continuity, the turbulence kinetic energy (k), and momentum (in the x, y, and z directions) were computed until all scaled residuals stabilized at a minimum value of 10^{-5}. Velocity and temperature were monitored at various points throughout the solving process to ensure convergence.

The model and its boundary conditions accurately reflect the actual architectural structure in terms of shape and size. As illustrated in Figure 5, the computational domain is represented as a rectangular prism with dimensions of 4.05 × 8.35 m and a vaulted ceiling with a maximum height of 4.68 m. A uniform velocity field was applied at the inlet (the building's door), with no-slip conditions enforced on all solid walls. The boundary conditions on walls adjacent to the external environment were set to variable temperatures within a stabilized periodic thermal regime. The flooring was treated as adiabatic, given its direct contact with the ground without any underground cavities. Lastly, an outlet boundary condition with uniform zero relative pressure was applied at the exit plane (the roof light of the building). The main characteristics of the building materials were also defined: the opaque walls have a density of 2800 kg/m^3, a specific heat capacity of 1000 J/kgK, and a thermal transmittance of 1.4 W/mK; the transparent roof light has a density of 120 kg/m^3, a specific heat capacity of 1000 J/kgK, and a thermal transmittance of 1 W/mK.

2.5.1. Mesh Sensitivity

The domain was discretized using an orthogonal grid, as depicted in Figure 5, which also shows the sensor locations. Given the relatively simple geometry, a block-based tetrahedral mesh was employed to improve the overall mesh quality. The grid was refined near the solid surfaces (building walls) and at the inlet and outlet, with the spacing between grid lines gradually increasing as they moved away from these surfaces. All inflation ratios of the mesh were maintained at 1.15. A mesh sensitivity analysis was conducted to assess the independence of the numerical solution from the mesh size, utilizing coarse, medium, and fine grids with 0.2, 0.8, and 2.2 million cells, respectively. The temperature recorded by one of the experimental measurement sensors (sensor number 66) was selected as the control parameter for this analysis.

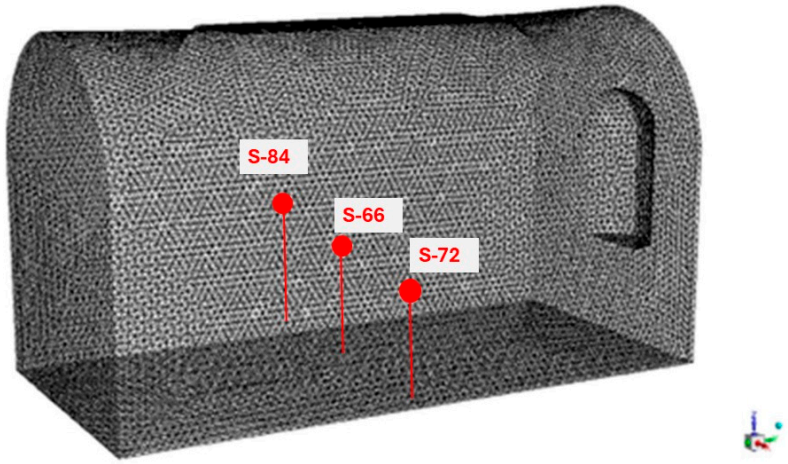

Figure 5. Domain mesh and sensor locations.

Assuming that the finest mesh (Mesh C—cell size of 0.05 m) was used as the pivot case, it can be observed that the temperature percentage difference Δ% on the probed point with Mesh A (cell size of 0.1 m) is only 3.20%. As shown in Table 4, Mesh A can be considered the best one because a further increase in the number of cells does not bring significant improvements (Δ% value is converging to 0) and can only increase the computational cost. Therefore, it was selected for the simulation in this paper. Furthermore, the Grid Convergence Index (GCI), which was developed by P.J. Boache for the assessment of mesh refinement [28], was applied to the different meshes, as reported in Table 4.

Table 4. Mesh sensitivity test.

	Mesh A	**Mesh B**	**Mesh C**
Number of cells [-]	~800,000	~200,000	~2,200,000
Cell spacing [m]	0.1	0.2	0.05
Δ% temperature [-]	3.15	15.72	-
GCI [%]	0.1	-	0.05

GCI can be expressed as follows [27]:

- Equation (1) provides the value of the convergence order p:

$$p = \frac{\frac{ln[\varphi_{average} - \varphi_{coarse}]}{\varphi_{fine} - \varphi_{average}}}{ln(r)} \quad (1)$$

where φ_{coarse}, $\varphi_{average}$, and φ_{fine} are, respectively, the average temperatures for the course, medium, and fine meshes.

- The mesh refinement ratio "r" can be calculated as shown in Equation (2) [28].

$$r = \left(\frac{N_{fine}}{N_{medium}}\right)^{1/D} \quad (2)$$

where N is the number of cells and D is the size of a single cell.

- GCI is calculated using Equations (3) and (4):

$$GCI = \frac{\epsilon}{r^p - 1} \quad (3)$$

$$\varepsilon = \left|\frac{\varphi_{fine} - \varphi_{medium}}{\varphi_{fine}}\right| \quad (4)$$

As shown in Table 4, all *CGI* values are below 1%, which confirms that the numerical results are independent of the grid [28].

2.5.2. Model Validation

This section outlines the validation process for the CFD model, which involves comparing the simulation results with experimental data to evaluate the overall quality of the simulation. Validation is essential in every CFD study, as it is the primary method for determining the accuracy and reliability of computational simulations [8]. For this case study, temperature and indoor humidity were selected as evaluation parameters, focusing on a single day, 10 August 2020, which experienced the most extreme atmospheric conditions in terms of temperature and humidity variability compared to all other days during the experimental campaign. The validation was conducted in a stabilized periodic regime to account for the building's thermal inertia and the daily fluctuations caused by the night–day cycle. The average simulated indoor temperature was 30.55 °C, with a range of ±6.25 °C. In contrast, humidity displayed less variability, remaining relatively stable with a mean value of 54.16% and a range of ±4.68%. Comparisons between the numerical simulations and the measured data are presented in Figures 6–8.

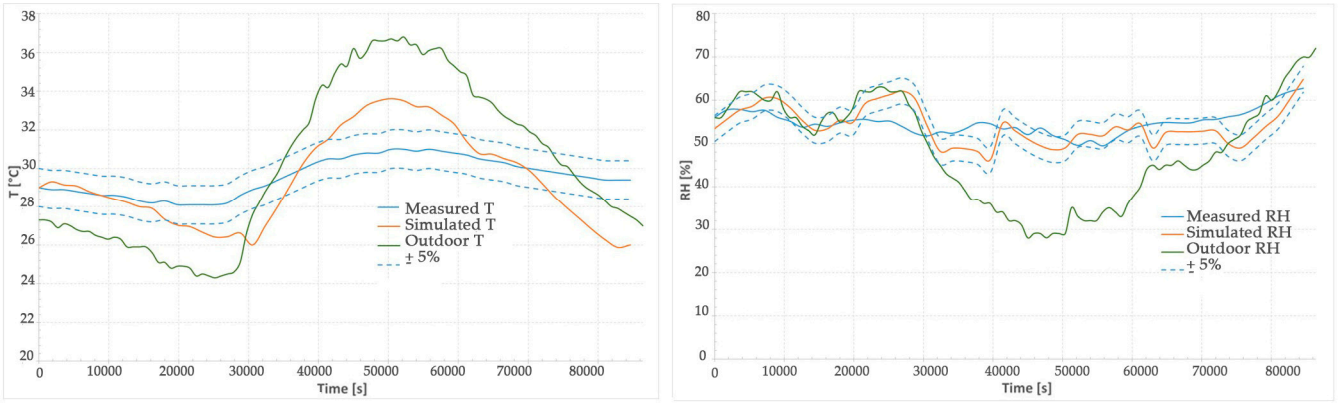

Figure 6. SENSOR 66: comparisons of temperature (**left**) and relative humidity (**right**) measured by the sensor, simulated, and registered outside the building.

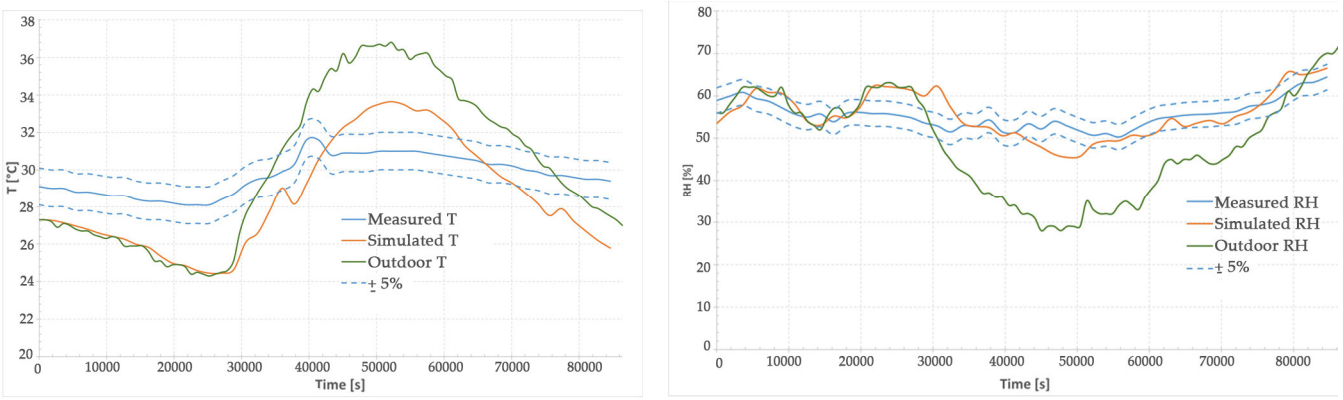

Figure 7. SENSOR 72: comparisons of temperature (**left**) and relative humidity (**right**) measured by the sensor, simulated, and registered outside the building.

As can be observed from the figures, the CFD model can reproduce the measured real conditions with good accuracy. The behavior of both the temperature and humidity are in line with the measured trends; the simulation average and maximum errors are reported in Table 5.

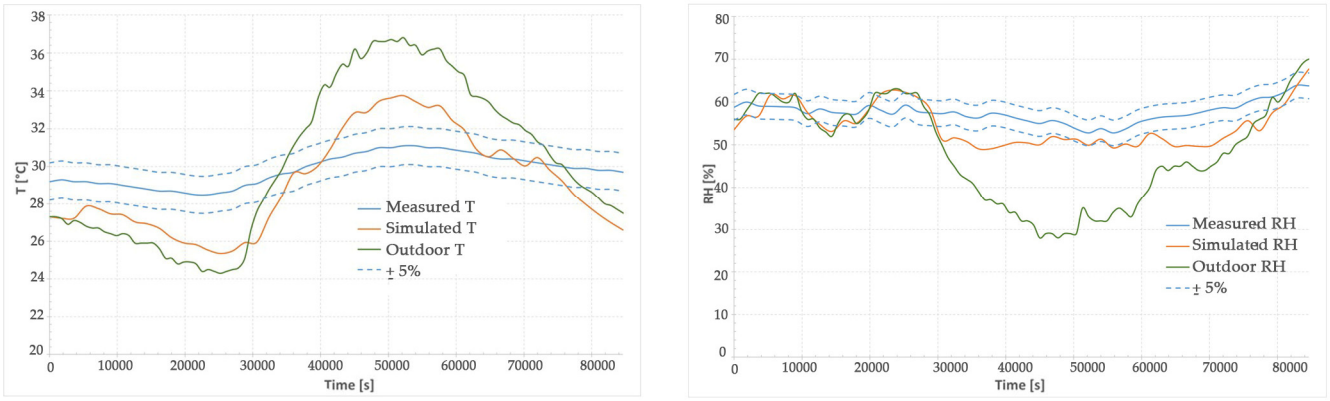

Figure 8. SENSOR 84: comparison of temperature (**left**) and relative humidity (**right**) measured by the sensor, simulated, and registered outside the building.

Table 5. Errors of the simulations performed.

		$\lvert T_{outdoor} - T_{CFD} \rvert$	$\lvert T_{indoor} - T_{CFD} \rvert$	$\lvert RH_{outdoor} - RH_{CFD} \rvert$	$\lvert RH_{indoor} - RH_{CFD} \rvert$
		[°C]	[°C]	[%]	[%]
Sensor 66	Max	7.60	3.70	21.46	9.34
	Average	2.25	2.26	7.82	2.36
Sensor 72	Max	7.60	4.30	21.91	10.49
	Average	2.25	2.41	7.85	2.89
Sensor 84	Max	7.60	3.80	22.59	9.32
	Average	2.25	2.51	7.76	3.57
Total	Max	7.60	4.30	22.59	10.49
	Average	2.25	2.40	7.81	2.94

Based on the data extracted from the simulations, the average error in the results can be considered as 5% for both temperature and humidity. Based on Table 5, the average errors from the simulation are approximately 2.33 °C for temperature and 5.38% for relative humidity. Given the relatively high maximum errors, the simulation is better suited to assessing the daily average thermal behavior of the building. These discrepancies may arise from the physical properties of the construction materials (particularly conductivity) being slightly different from their actual values. Notably, the indoor and outdoor measurements exhibit different trends in temperature and relative humidity, indicating that the structure has high thermal inertia. This means that indoor conditions tend to remain stable throughout the day, responding with a delay to external influences. This is expected, considering that the average wall thickness is about 0.6 m, which is typical of many historical buildings [29]. Temperature and relative humidity maps are shown in Figure 9, referencing the time at which humidity peaks. Additional figures (A1 to A3) displaying the velocity vector results and cross-sectional data (humidity, temperature, and velocity) can be found in the Electronic Supplementary Material (ESM).

The phenomena of natural convection, wherein the hot air rises, is visible in Figure 9. The section shows natural convective motion, with colder air near the wall and hot air coming from the floor. As visible in the figures, areas with high temperatures have a lower relative humidity and vice versa. This phenomenon, if not managed correctly, can lead to humidity rising from the floor and walls, causing the deposition of dissolved salts where humidity is lower and mold growth where the temperature is higher [30–32].

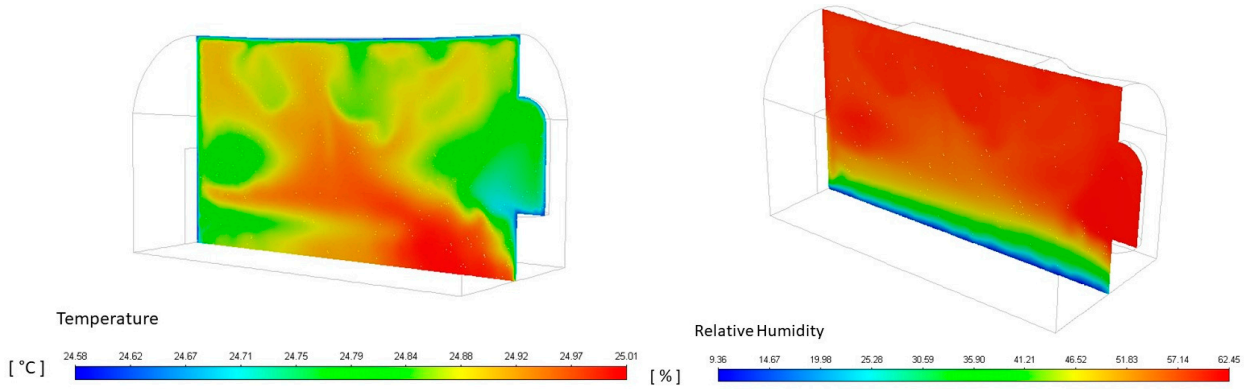

Figure 9. Temperature (**left**) and relative humidity (**right**) results on the longitudinal section.

2.6. Simulated Conditions

The technical specifications of the electrical transformer enclosure are outlined in Table 6. The proposed ventilation system has a total electrical power of 3250 W and can achieve flow rates of up to 2200 m^3/h. For the simulations, two flow rates were selected: a minimum of 1100 m^3/h and a maximum of 2200 m^3/h. Additionally, the ventilation system must ensure that the indoor temperature remains below 40 °C, and that the air velocity does not exceed 6 m/s in the main ducts and 4.5 m/s in the secondary ducts.

Table 6. Electrical transformer enclosure characteristics.

Type of Power Supply	Power	Frequency	Three Phase Voltage	Distribution System	Neutral State
MT	500 kW	50 Hz	20 kV/400 V ± 5%	TN-S	Distributed

Two possible scenarios can be considered for the transformer enclosure installation: a confined layout, with the transformer enclosure insulated from the indoor environment using panes, and an open layout, with the transformer enclosure simply placed at the center of the building. The layouts will be described in detail in Paragraph 2.6.1. A total of 6 simulations were performed, as can be seen in Table 7.

Table 7. Simulation layouts and mass flow rate.

Simulation	Electronic Supplementary Material (ESM)	Layout	Mass Flow Rate
C-1	Only velocity results	Confined transformer enclosure	1100 m^3/h
C-2	All data		1650 m^3/h
C-3	All data		1925 m^3/h
C-4	Only velocity results		2200 m^3/h
O-1	Only velocity results	Open layout	1100 m^3/h
O-2	Only velocity results		2200 m^3/h

Simulations C-2 and C-3 will not be discussed in this paper but are reported in the ESM (Figures S20–S27). The decision to include these simulations in the ESM is due to their intermediate behavior compared to C-1 and C-4, which is not worth a dedicated discussion considering the inadequate results obtained at the maximum flow rate. The other imposed boundary conditions are reported in Table 8 and are the same for each simulation (open and close layout and mass flow rate).

The conditions were chosen based on the worst-case scenario measured during the experimental campaign. In the numerical model, the cabin was modelled by using the heat source that emits the real load in the cabin (3250 W).

Table 8. Boundary conditions used in each simulation.

Boundary Conditions	Location	Value
External temperature	All walls and ceiling	36.7 °C
Air temperature	Inlet air grille	36.7 °C
Adiabatic	Floor	-
Relative humidity	Inlet air	48.78%
Pressure outlet	Skylight	1 atm

Simulated Conditions

Figure 10a illustrates the layout of the open transformer enclosure without the air extraction system. Figure 10b shows the air extraction system applied to this layout. The system includes a duct network with an air extraction fan located on the ceiling. Fresh air is drawn in from outside through a grated opening in the entrance door. Air extraction occurs by pushing the air through an opening in the grate positioned above the entrance door (see Figure 10b).

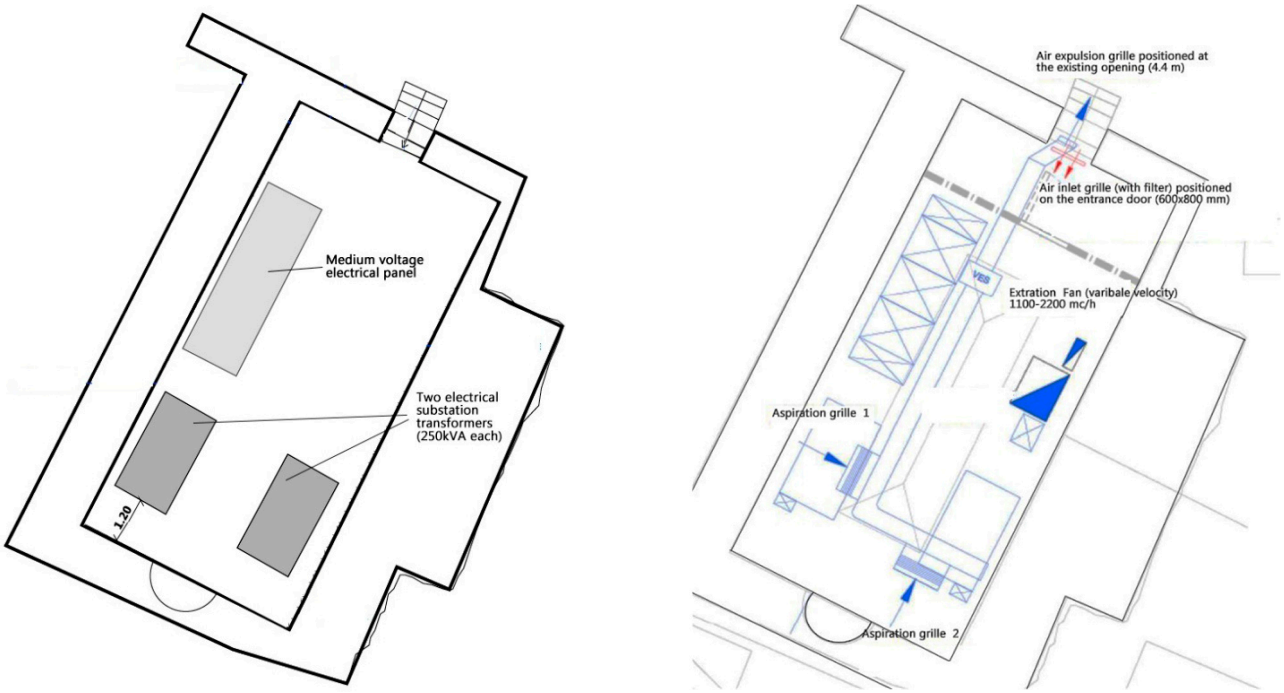

(**a**) (**b**)

Figure 10. (**a**) Technical system of air extraction in layout one (open transformer enclosure); (**b**) layout of the open transformer enclosure.

The confined layout utilizes a specialized enclosure (Figure 11a) constructed from rigid foam insulation panels that are 8.0 cm thick, with a thermal conductivity of 0.026 W/m·K [33–35]. This envelope is designed to shield the building from thermal stress resulting from the energy dissipated by the electrical equipment in the transformer enclosure. Additionally, the design of the panels facilitates the direct inspection of the transformer enclosure, as they can be moved along rails for easy access to the interior. This feature is crucial for ensuring maintenance access while keeping the two environments as separate as possible. In this layout, the air ducts connect to the internal environment of the transformer enclosure through a dedicated pipeline (Figure 11b).

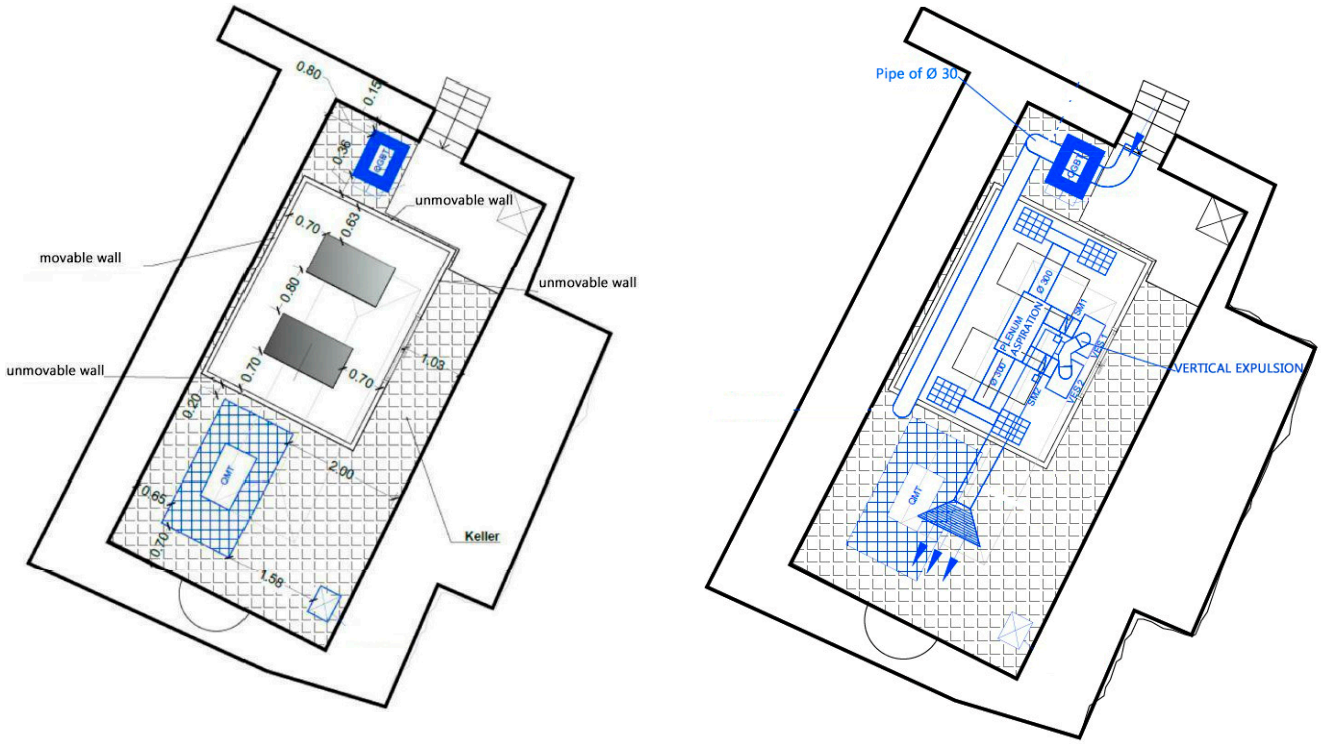

(**a**) (**b**)

Figure 11. (**a**) Layout of the open transformer enclosure; (**b**) layout of the confined transformer enclosure.

3. Results

Separate simulations were conducted for each condition and configuration, as detailed in Table 7. The layouts were modelled based on the volumes depicted in Figures 10 and 11. To ensure the convergence of the simulations, a scaled residuals threshold of 10^{-5} was applied for continuity, turbulence kinetic energy (k), and momentum in the x, y, and z directions. The simulations for the open transformer enclosure considered both the temperature and relative humidity at the sensor locations (66, 72, and 84), utilizing longitudinal and transverse sections positioned at the building center, with a height of 1.50 m. For the closed transformer enclosure layout, this was not feasible due to the coverage of the transformer enclosure at those locations. Thus, only the orthogonal sections taken at the same positions as the open transformer enclosure layout are presented. All temperature and relative humidity data correspond to the worst-case scenario when temperatures peak at the three sensor locations. The discussion will begin with the open transformer enclosure layout, followed by the closed layout, highlighting the main advantages and disadvantages of both configurations. For brevity, the results from sensors 72 and 84 are included in the ESM document (Figures S4, S5, S9 and S10). Additionally, the velocity results for both layouts in the longitudinal section (Figures S6, S11, S14 and S17) and the simulations for the transverse sections (Figures S7, S8, S12, S13, S15–S18) are compiled in the ESM.

3.1. Open Transformer Enclosure

3.1.1. Minimum Flow

The simulation results presented in Figure 12 pertain to Sensor 66, located in the center of the room, and thus reflect the primary variations in the indoor environment. The results for Sensors 84 and 72 can be found in the Electronic Supplementary Material (Figures S4, S5, S9 and S10). Case O-1 features an airflow rate of 1100 m^3/h. It is evident that the presence of the transformer enclosure significantly alters the indoor thermo-hygrometric conditions, leading to a marked increase in temperature and a decrease in humidity. More-

over, these findings indicate that the air extraction system is inadequate for keeping the temperature within the operational limits required for the transformers.

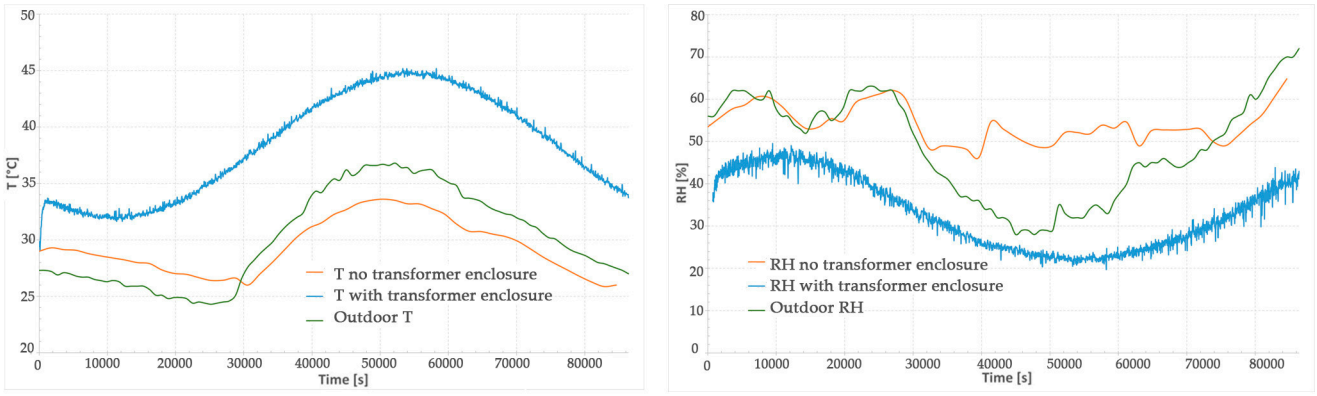

Figure 12. Simulation O-1, Sensor 66: temperature (**left**) and relative humidity (**right**) results.

According to the simulation results, the CFD probe placed at the position of Sensor 66 (center of the room) registers an increase in the indoor temperature of about 8 °C due to the heat produced by the electrical transformer enclosure. The relative humidity decreases up to 22–23% (Figure 12). Figure 13 shows a graphic representation of the indoor temperature and relative humidity values on the section plane placed at the center of the building. The increase in temperature close to the electrical transformer can be noted.

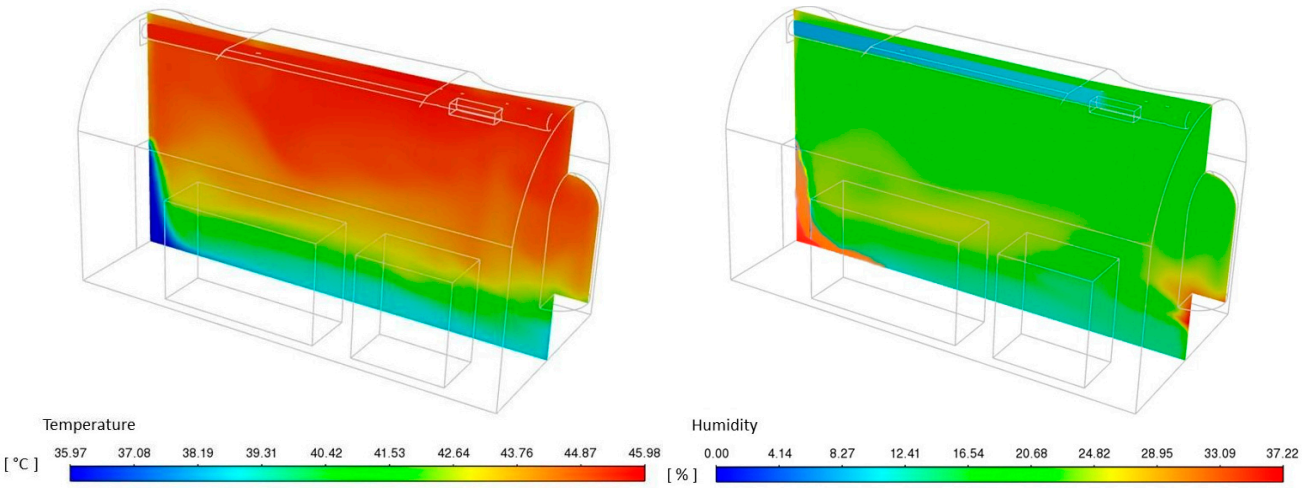

Figure 13. Simulation O-1: Temperature and relative humidity fields on the lateral plane.

Figure 13 illustrates the phenomenon of natural stratification, where warm air accumulates near the ceiling above cooler air. The humidity levels within the indoor environment can fluctuate up to 29%, with the lowest values observed near the electrical transformers. This decrease in humidity is associated with the rise in temperature and could lead to moisture rising up from the ground and walls, potentially resulting in saline deposits that may damage the plaster. Additionally, the humidity and temperature plume emanating from the door are visible in Figure 13; this plume is a result of air being drawn in by the extraction fan. Beneath this plume, air circulation is minimal, and the humidity levels are close to zero.

3.1.2. Maximum Flow

The second presented result (O-2) is for the open layout at a maximum airflow rate of 2200 m^3/h. First, the trend is presented (Figure 14), followed by the fields obtained in the section (Figure 15). The probe at the position of Sensor 66 registers a maximum temperature of up to 40 °C and a relative humidity minimum of 25% (Figure 14).

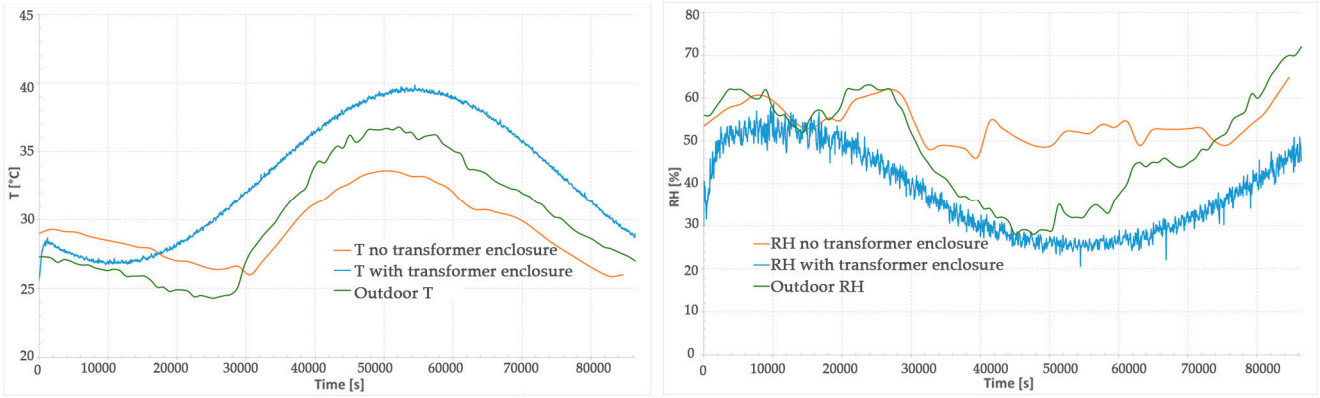

Figure 14. Simulation O-2, Sensor 66: temperature (**left**) and relative humidity (**right**) results.

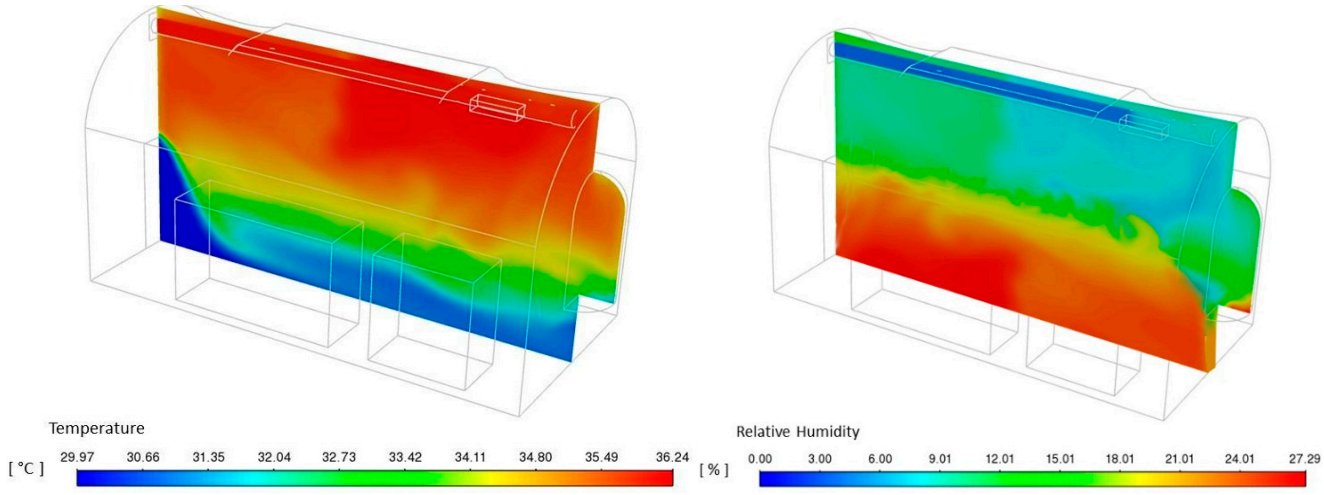

Figure 15. Simulation O-2: Temperature (**left**) and relative humidity (**right**) fields on the longitudinal plane.

The temperature and relative humidity fields of the sections are shown in Figure 15. A uniform increase in the indoor temperature is visible in the whole environment. This uniformity is due to the higher mass flow rate of extraction if compared to O-1. The presence of an extraction fan causes a higher stratification in temperature instead of creating circulation vortexes; this is because the hot air is taken uniformly by the ducts all over the ceiling, and not from a single extraction point (Figure 15). The ventilation system is barely sufficient to guarantee the operation of the transformers, but the low humidity makes this solution inappropriate for a historical building. Moving to the relative humidity field, the section shows a moderate gradient. The lower values are registered at the ceiling.

3.2. Confined Transformer Enclosure Layout

3.2.1. Minimum Flow

Figure 16 displays the temperature and relative humidity fields generated from simulation C-1. In this configuration, a comparative analysis using the sensor positions from the measurement campaign was not feasible, as their locations are obscured by the transformer enclosure. The airflow rate for this simulation is set at 1100 m^3/h, the lowest among the analyses, making C-1 a worst-case scenario for the confined transformer enclosure layout. As shown in Figure 16, the enclosure effectively isolates the air within the transformer enclosure from that in the surrounding room, allowing for different temperatures and humidity levels in each space. The average temperature inside the confined area reaches approximately 41 °C, which exceeds the operational limit of 40 °C. Thus, this airflow rate is insufficient for summer use but could be suitable during other seasons, conserving energy for the fan system. Additionally, comparing the building's temperatures and humidity

levels with those recorded without the electrical transformer enclosure shows that they align with the inlet conditions (36.7 °C and 48.78% RH). Consequently, this layout proves optimal for preserving the building, as it ensures that the indoor environment is consistent with the outdoor conditions [36].

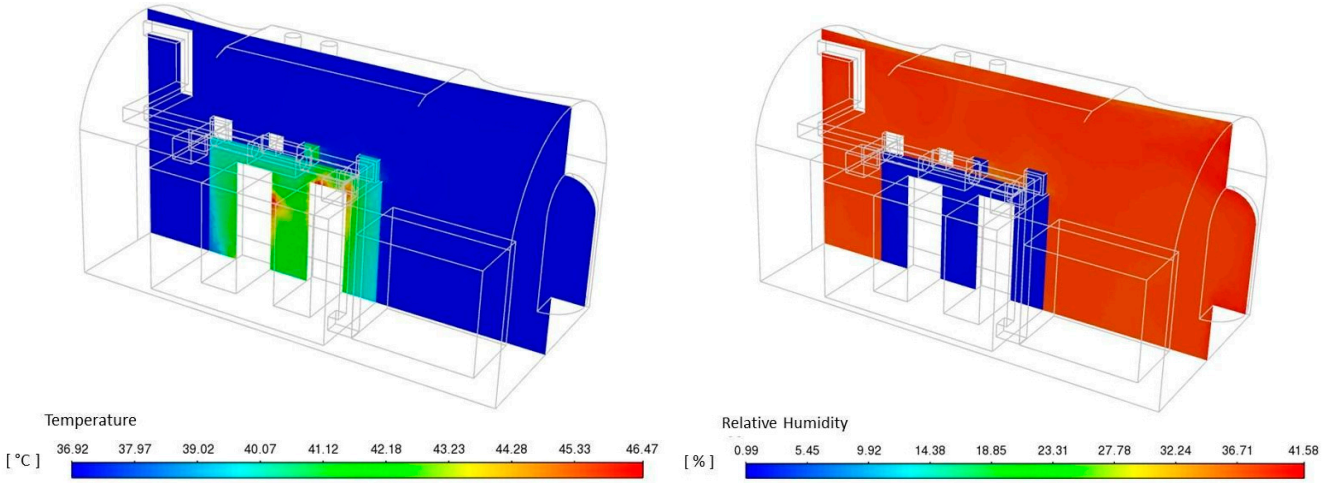

Figure 16. Simulation C-1: Temperature (**left**) and relative humidity (**right**) fields on the longitudinal plan.

3.2.2. Maximum Flow

The results from the C-4 simulation are presented in Figure 17. This simulation was conducted to compare the operational ranges of the closed transformer enclosure layout at both minimum and maximum airflow rates. In this case, the airflow rate is increased to its maximum value of 2200 m^3/h. The average temperature within the transformer enclosure remains relatively uniform at around 39 °C, which is below the operational threshold of 40 °C. Similar to the C-1 scenario, the temperatures and relative humidity outside the confined space match the inlet air temperature. This consistency is attributed to the physical separation of the two environments and the effective insulating properties of the panels.

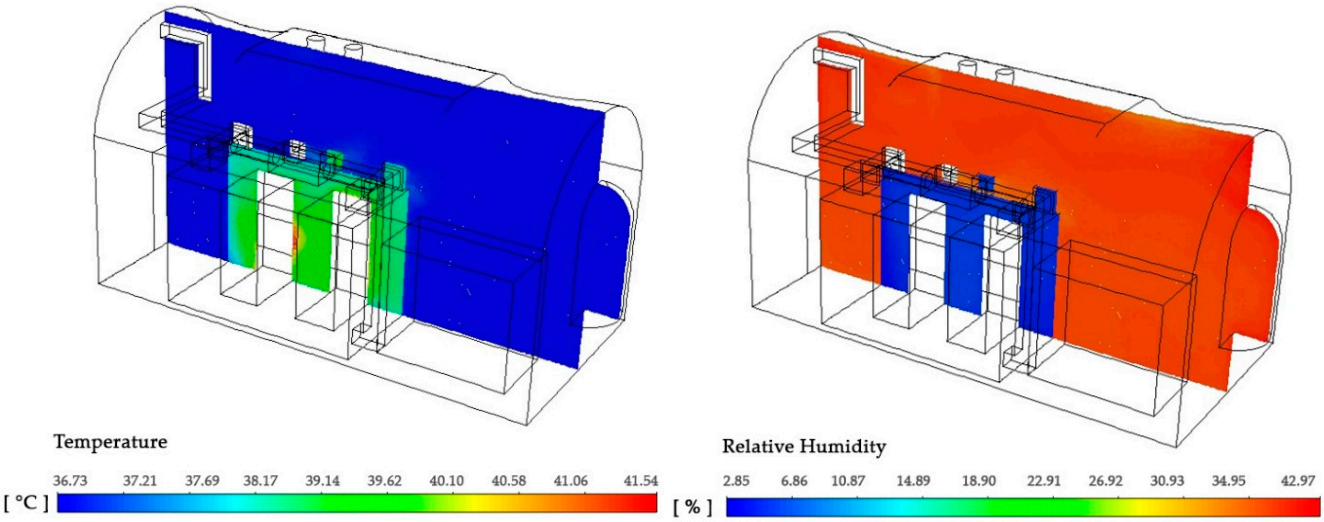

Figure 17. Simulation C-4: Temperature (**left**) and relative humidity (**right**) fields on the longitudinal plan.

In conclusion, the closed transformer enclosure configuration is effective for preserving the building and accommodating an electrical power transformer. However, there are drawbacks to consider. For instance, the separation of the two environments may delay response times in the event of failures, complicating maintenance efforts. Additionally, the fans could generate noise during the summer, which may be audible in the surrounding

areas of the building. Lastly, the costs associated with this configuration are higher, making it a viable option primarily for historically significant structures.

4. Discussion

The experimental campaign was performed in the period from July to September when the temperatures in the site were higher. The maximum recorded outdoor temperature was 39 °C, with an average of 27.7 °C. The maximum recorded temperature measured inside the building was 34 °C on the northwest-facing wall, and the average indoor temperature measured at the center of the building was 28 °C. The maximum solar radiation power was 928 W/m^2 and the average daily value was 573.6 W/m^2. For the relative humidity, its outdoor peak was 91% RH, measured during a rainy day, and the average was 58% RH. Inside the building, the maximum value was 71% RH, with an average of 58%RH. Considering the need to maintain the air temperature around the transformer at a maximum of 40 °C, it is necessary to install a forced ventilation system to mitigate the rise in temperature due to the power produced inside the environment. Therefore, in this study, two different layouts are proposed (open and con-fined transformer enclosures) and a total of five simulations were performed at different mass flow rates, as shown in Table 7. To avoid overtreatment, only the maximum and minimum possible air-flow rates are discussed (1100 and 2200 m^3/h); the others are available in the ESM document. The boundary conditions used were obtained from the measurement campaign data, considering an inlet air with a temperature of 36.7 °C and a humidity of 48.7%RH.

The open layout, with the transformer enclosure placed inside the building and cooled by air with an extraction fan system, shows bad performances in terms of temperature and humidity inside the building. The humidity notability decreases and the temperature rises compared to the external air temperature. This would lead to water rising from the walls, which can cause saline formations. At the same time, when the humidity is high and the temperature is lower, water can condense, allowing molds and fungi to grow. Therefore, this layout is not suitable for a historical building. Higher temperatures are reached on the ceiling when the temperature reaches ~46 °C and the humidity reaches ~37% RH when the air flow rate is 1100 m^3/h. These conditions are far from optimal, resulting in temperatures that are too high and possible damage to the plasters and the transformer itself. At a flow rate of 2200 m^3/h, the maximum indoor temperature is ~36 °C, but there is a humidity value of ~27%RH. Considering that the humidity of the inlet air is 48.78% RH, this results in a very high variation that can lead to the capillary rise of water on plasters and the consequent formation of saline formations. At the same time, when humidity is high and the temperature is lower, water can condense, allowing mold and fungal growth. Therefore, this layout is not suitable for a historical building.

The second layout considers installing the transformer enclosure inside a paneled enclosure to physically separate the power transformer from the building interior. In this case, the cooling air is extracted from the enclosure by the same ventilation system as the open layout. Analyzing the results, this layout showed rather good performance, both in insulating the transformer enclosure interior from the building environment and in maintaining the temperatures inside the operative range. At the maximum flow rate, the transformer enclosure operates under 39 °C, and at minimum flow, the transformer enclosure's average temperature is 41 °C, slightly over the required 40 °C. Both cases allow for the preservation of the building, maintaining microclimatic indoor conditions at the same level as the external temperatures and humidities. Therefore, this layout is optimal for the preservation of the building because it does not alter the indoor environment and maintains the same environmental conditions as the outdoor environment [37]. However, there are also some downsides to consider. For example, separating the two environments delays the intervention time in the case of failures, making the maintenance process more complex. Moreover, fans could make noise during summer, which can be heard in the building's proximity. Finally, the costs related to this configuration are higher, and this makes this solution suitable only in the case of buildings of historic importance.

5. Conclusions

This study has been developed to investigate a feasible solution to host an electrical power transformer enclosure inside a historical building with a reuse intervention. The site selected is made of a single room and it is supposed to have been built during the 3rd century A.D. Its preservation is of fundamental importance, and the requirements for such installation are clear; the indoor microclimatic conditions shall not be modified, to avoid the formation of molds or saline formations over the plasters. High temperatures combined with high thermal gradients can cause the detachment of plaster. At the same time, the transformer enclosure's transformers must work at low temperatures, to avoid damage and malfunctions.

The impact of the transformer enclosure on the microclimatic indoor parameters was therefore studied by CFD simulations, with five different simulations and two different layouts of the transformer enclosure. The simulations were validated using data obtained from a measurement field campaign performed during summer, from July to September. As hypotheses for the simulations were formulated, the worst-case conditions were recorded during the campaign (36.7 °C of air temperature and a humidity of 48.7% RH). The inlet air flow rate varied from 1100 and 2200 m^3/h. In this work, only the minimum and maximum flow rates are discussed, leaving the other cases (1650 m^3/h and 1925 m^3/h) in the ESM document. The two layouts use the same boundary conditions but differ in the presence of a confining box containing the power transformer in the second case. The box is made of rigid foam insulation panels with a thickness of 8.0 cm and is designed to protect the building from the thermal stress caused by the rise in temperature due to the transformer power dissipating into the environment. Both layouts use an inlet fan to cool the transformer, but in the second case, the ventilation is directed inside the box by a duct system.

The results showed good performances for the confined solution, which can maintain indoor temperature and humidity in an acceptable range for both the historical building and the power transformer, while the open layout is unable to maintain a good condition for both the maximum and minimum air-flow rates. Moreover, in the first layout, the simulated microclimatic conditions do not ensure the proper preservation of the building. The humidity notably decreases as the temperature rises compared to the external air temperature.

In conclusion, this study aims to present a specific case where an electrical transformer enclosure is installed inside a historical building. From the analysis, to ensure the preservation of the building as well as the performance of the electrical transformer enclosure, confinement appears to be the best solution so as not to alter the internal microclimate conditions.

Supplementary Materials: The following supporting information can be downloaded at: https://www.mdpi.com/article/10.3390/app142310827/s1, File S1: Electronic Supplementary Material (ESM).

Author Contributions: Conceptualization, F.N. and L.G.; Data curation, L.G.; Formal analysis, F.N. and L.P.; Funding acquisition, F.N. and L.G.; Investigation, F.N., L.G. and L.P. Methodology, F.N., L.G. and L.P.; Project administration, F.N., L.G. and F.C.; Resources, L.G.; Software, F.N. and L.P.; Supervision, F.N., L.G. and F.C.; Validation, F.N., L.G. and L.P.; Visualization, F.N., L.G., L.P. and F.C.; Writing—original draft, F.N., L.G. and L.P. Writing—review and editing, F.N. and L.P. All authors have read and agreed to the published version of the manuscript.

Funding: This research received no external funding.

Institutional Review Board Statement: Not applicable.

Informed Consent Statement: Not applicable.

Data Availability Statement: The original contributions presented in the study are included in the article/Supplementary Material, further inquiries can be directed to the corresponding author.

Conflicts of Interest: The authors declare no conflicts of interest.

References

1. Bay, E.; Martinez-Molina, A.; Dupont, W.A. Assessment of Natural Ventilation Strategies in Historical Buildings in a Hot and Humid Climate Using Energy and CFD Simulations. *J. Build. Eng.* **2022**, *51*, 104287. [CrossRef]
2. Pompei, L.; Nardecchia, F.; Bisegna, F. A New Concept of a Thermal Network for Energy Resilience in Moun-tain Communities Powered by Renewable Sources. *Sustain. Energy Grids Netw.* **2023**, *33*, 100980. [CrossRef]
3. Fayez, H. From 'Objects' to 'Sustainable Development': The Evolution of Architectural Heritage Conserva-tion in Theory and Practice. *Buildings* **2024**, *14*, 2566. [CrossRef]
4. *Presidente Della Repubblica Decreto Legislativo 22 Gennaio 2004, n. 42 "Codice Dei Beni Culturali e Del Pae-Saggio"*; CWL Publishing Enterprises, Inc.: Madison, WI, USA, 2004.
5. Camuffo, D.; Grieken, V.; Busse, H.-J.; Sturaro, G.; Valentino, A.; Bernardi, A.; Blades, N.; Shooter, D.; Gysels, K.; Deutsch, F.; et al. Environmental Monitoring in Four Europe-an Museums. *Atmos. Environ.* **2001**, *35*, S127–S140. [CrossRef]
6. Martínez-Molina, A.; Tort-Ausina, I.; Cho, S.; Vivancos, J.L. Energy Efficiency and Thermal Comfort in Historic Buildings: A Review. *Renew. Sustain. Energy Rev.* **2016**, *61*, 70–85. [CrossRef]
7. Varas-Muriel, M.J.; Fort, R. Microclimatic Monitoring in an Historic Church Fitted with Modern Heat-ing: Implications for the Preventive Conservation of Its Cultural Heritage. *Build Environ.* **2018**, *145*, 290–307. [CrossRef]
8. Balocco, C.; Grazzini, G. Numerical Simulation of Ancient Natural Ventilation Systems of Historical Buildings. A Case Study in Palermo. *J. Cult. Herit.* **2009**, *10*, 313–318. [CrossRef]
9. Li, Y.; Chen, L.; Yang, L. CFD Modelling and Analysis for Green Environment of Traditional Buildings. *Energies* **2023**, *16*, 1980. [CrossRef]
10. Rook, T. The Development and Operation of Roman Hypocausted Baths. *J. Archaeol. Sci.* **1978**, *5*, 269–282. [CrossRef]
11. Bean Robert, O.W.B.K.W.K. Bean_2010_History-of-Radiant-Heating-e-Cooling-Systems. Available online: www.ashrae.org (accessed on 11 November 2024).
12. Bean, R.; Olesen, B.W. Part 1: History of Radiant Heating & Cooling Systems; Part 2: History of Radiant Heating & Cooling Systems View Project International Energy Agency Energy in Buildings and Commu-nities Programme, Annex 66, Definition and Simulation of Occupant Behavior in Buildings. *APT Bull.* **1996**, *27*, 12–24.
13. Brown, J.P.; Rose, W.B. Development of Humidity Recommendations in Museums and Moisture Control in Buildings. *APT Bull.* **1996**, *27*, 12–24. [CrossRef]
14. Rosina, E. When and How Reducing Moisture Content for the Conservation of Historic Building. A Problem Solving View or Monitoring Approach? *J. Cult. Herit.* **2018**, *31*, S82–S88. [CrossRef]
15. Aktas, Y.D.; Shi, J.; Blades, N.; D'Ayala, D. Indoor Mould Testing in a Historic Building: Blickling Hall. *Herit. Sci.* **2018**, *6*, 51. [CrossRef]
16. Hajdukiewicz, M.; Geron, M.; Keane, M.M. Formal Calibration Methodology for CFD Models of Natu-rally Ventilated Indoor Environments. *Build. Envion.* **2013**, *59*, 290–302. [CrossRef]
17. Corgnati, S.P.; Perino, M. CFD Application to Optimise the Ventilation Strategy of Senate Room at Palazzo Madama in Turin (Italy). *J. Cult. Herit.* **2013**, *14*, 62–69. [CrossRef]
18. Balocco, C.; Grazzini, G. Plant Refurbishment in Historical Buildings Turned into Museum. *Energy Build.* **2007**, *39*, 693–701. [CrossRef]
19. Abuku, M.; Janssen, H.; Roels, S. Impact of Wind-Driven Rain on Historic Brick Wall Buildings in a Moderately Cold and Humid Climate: Numerical Analyses of Mould Growth Risk, Indoor Climate and Energy Consumption. *Energy Build.* **2009**, *41*, 101–110. [CrossRef]
20. Gagliano, A.; Liuzzo, M.; Margani, G.; Pettinato, W. Thermo-Hygrometric Behaviour of Roman Ther-mal Buildings: The "Indirizzo" Baths of Catania (Sicily). *Energy Build.* **2017**, *138*, 704–715. [CrossRef]
21. Balocco, C. Daily Natural Heat Convection in a Historical Hall. *J. Cult. Herit.* **2007**, *8*, 370–376. [CrossRef]
22. Blocken, B.; Roels, S.; Carmeliet, J. A Combined CFD-HAM Approach for Wind-Driven Rain on Build-ing Facades. *J. Wind Eng. Ind. Aerodyn.* **2007**, *95*, 585–607. [CrossRef]
23. La Gennusa, M.; Rizzo, G.; Scaccianoce, G.; Nicoletti, F. Control of Indoor Environments in Heritage Buildings: Experimental Measurements in an Old Italian Museum and Proposal of a Methodology. *J. Cult. Herit.* **2005**, *6*, 147–155. [CrossRef]
24. Holm, A.; Kuenzel, H.M.; Sedlbauer, K. The hygrothermal behaviour of rooms: Combining thermal building simulation and hygrothermal envelope calculation. In Proceedings of the Eighth International ibpsa Conference, Eindhoven, The Netherlands, 11–14 August 2003.
25. Papakonstantinou, K.A.; Kiranoudis, C.T.; Markatos, N.C. Computational Analysis of Thermal Comfort: The Case of the Archaeological Museum of Athens. *Appl. Math. Model.* **2000**, *24*, 477–494. [CrossRef]
26. Pagliaro, F.; Nardecchia, F.; Gugliermetti, F.; Bisegna, F. CFD Analysis for the Validation of Archaeo-logical Hypotheses—The Indoor Microclimate of Ancient Storage-Rooms. *J. Archaeol. Sci.* **2016**, *73*, 107–119. [CrossRef]
27. Nardecchia, F.; Mattoni, B.; Pagliaro, F.; Cellucci, L.; Bisegna, F.; Gugliermetti, F. Computational Fluid Dynamic Modelling of Thermal Periodic Stabilized Regime in Passive Buildings. *Sustainability* **2016**, *8*, 1172. [CrossRef]
28. Carandini, A.; Carafa, P.; D'Alessio, M.T.; Filippi, D. *Santuario Di Vesta, Pendice Del Palatino e Via Sacra. Scavi 1985–2016*, 1st ed.; Edizioni Quasar: Rome, Italy, 2017; Volume 1.

29. Buranelli Le Pera, S.; D'Elia, L. «Sacra Via»: Note Topografiche. In *Bullettino della Commissione Archeologica Comunale di Roma*; L'Erma di Bretschneider: Rome, Italy, 1986; Volume 2.
30. Moretti, M. *La Camera Degli Sposi 1958 Prima Edizione*, 1st ed.; Mondadori: Verona, Italy, 1958; Volume 1.
31. Boache, P.J. Perspective: A Method for Uniform Reporting of Grid Refinement Studies. *J. Fluids Eng.* **1994**, *116*, 405–413.
32. Yüksel, A.; Arici, M.; Karabay, H. Comparison of Thermal Response Times of Historical and Modern Building Wall Materials. *J. Therm. Eng.* **2021**, *7*, 1506–1518. [CrossRef]
33. Lourenço, P.B.; Luso, E.; Almeida, M.G. Defects and Moisture Problems in Buildings from Histori-cal City Centres: A Case Study in Portugal. *Build. Environ.* **2006**, *41*, 223–234. [CrossRef]
34. Johansson, P.; Ekstrand-Tobin, A.; Svensson, T.; Bok, G. Laboratory Study to Determine the Critical Moisture Level for Mould Growth on Building Materials. *Int. Biodeterior. Biodegrad.* **2012**, *73*, 23–32. [CrossRef]
35. Lazo, M.; Puga, I.; Macías, M.A.; Barragán, A.; Manzano, P.; Rivas, A.; Rigail-Cedeño, A. Mechanical and Thermal Properties of Polyisocyanurate Rigid Foams Reinforced with Agricultural Waste. *Case Stud. Chem. Environ. Eng.* **2023**, *8*, 100392. [CrossRef]
36. d'Ambrosio Alfano, F.R.; Palella, B.I.; Riccio, G. Moisture in Historical Buildings from Causes to the Application of Specific Diagnostic Methodologies. *J. Cult. Herit.* **2023**, *61*, 150–159. [CrossRef]
37. Xiong, J.; Li, A.; Liu, C.; Dong, J.; Yang, B.; Cao, J.; Ren, T. Probing the Historic Thermal and Humid Environment in a 2000-Year-Old Ancient Underground Tomb and Enlightenment for Cultural Her-itage Protection and Preventive Conservation. *Energy Build.* **2021**, *251*, 111388. [CrossRef]